PONTIFICIA UNIVERSIDAD CATOLICA DE CHILE
SCHOOL OF ENGINEERING

CHEMICAL SPECIES SEPARATION IN MRI WITH SIMULTANEOUS ESTIMATION OF FIELD MAP AND T_2^* USING A k–SPACE FORMULATION

JOSÉ LUIS HONORATO LIRA

Thesis submitted to the Office of Research and Graduate Studies
in partial fulfillment of the requirements for the degree of
Master of Science in Engineering

Advisor:
PABLO IRARRÁZAVAL M.

Santiago de Chile, August 2011

PONTIFICIA UNIVERSIDAD CATOLICA DE CHILE
SCHOOL OF ENGINEERING

CHEMICAL SPECIES SEPARATION IN MRI WITH SIMULTANEOUS ESTIMATION OF FIELD MAP AND T_2^* USING A k–SPACE FORMULATION

JOSÉ LUIS HONORATO LIRA

Members of the Committee:
PABLO IRARRÁZAVAL M.
CRISTIAN TEJOS N.
MATÍAS COURDURIER B.
IGNACIO CASAS R.

Thesis submitted to the Office of Research and Graduate Studies
in partial fulfillment of the requirements for the degree of
Master of Science in Engineering

Santiago de Chile, August 2011

Gratefully to my family

ACKNOWLEDGEMENTS

In a few words I would like to acknowledge all the people that supported and contributed to this work. First and foremost, I would like to thank my advisor, Prof. Pablo Irarrázaval, for his constant advice and for sharing his knowledge. His eagerness for doing high quality cutting-edge research in our group has been crucial for my education as an engineer and as a person.

I am truly thankful to Vicente Parot for his support and professionalism, his input has been decisive for the development of this work. For the people working at the Biomedical Imaging Center, Prof. Cristián Tejos, Prof. Sergio Uribe, Prof. Claudia Prieto, Prof. Matías Courdurier, Cristóbal, Allan, Carlos, Tomás, Edson and my engineering colleagues, my most sincere gratitude for your advice and friendship. I would also like to thank CONICYT for their funding through the grants FONDECYT 1070674 and 1100529 and ANILLO PBCT-ACT-79.

Finally, I am completely grateful to my family; my parents Blanca and José Luis, my brothers and sisters Blanquita, Trinidad, Raimundo, Francisca, Santiago and Elisa, and also Valentina, for their immense love and support. This thesis is dedicated to them.

TABLE OF CONTENTS

LIST OF TABLES

LIST OF FIGURES

ABSTRACT

Chemical species separation techniques in image space are prone to incorporate several distortions. Some of these are signal accentuation in borders and geometrical warping from field inhomogeneity. These errors come from neglecting intra-echo time variations. In this work we present a new approach for chemical species separation in MRI with simultaneous estimation of field map and T_2^* decay, formulated entirely in k–space. In this approach, the time map is used to model the phase accrual from off-resonance precession, and also the amplitude decay due to T_2^*. Our technique fits the signal model directly in k–space with the acquired data minimizing the l_2-norm with an interior-point algorithm. Standard 2D gradient echo sequences in the thighs and head were used for demonstrating the technique. With this approach we were able to obtain excellent estimation for the species, the field inhomogeneity and T_2^* decay images. The results do not suffer from geometric distortions derived from the chemical shift or the field inhomogeneity. Importantly, since the T_2^* map is well positioned, the species signal in borders is correctly estimated. Considering intra-echo time variations in a complete signal model in k–space for separating species yields superior estimation of the variables of interest when compared to existing methods.

Keywords: Magnetic Resonance Imaging, Chemical Species Separation, Fat and Water, Field Inhomogeneities, Off–Resonance Correction, R_2^* map.

RESUMEN

Separar diferentes especies químicas en imágenes de resonancia magnética (MRI) es relevante en el diagnóstico de pacientes, ya que permite identificar estructuras que típicamente resultan opacadas en imágenes comunes. Se han logrado buenos resultados con algoritmos en el espacio de la imagen, incluyendo en el modelo de señal parámetros de decaimiento transversal (R_2^*) y modelo multipico del espectro de la grasa. Sin embargo, separar especies en el espacio de la imagen, es decir, asumiendo un tiempo de adquisición instantáneo, causa artefactos en las imágenes resultantes. Algunos esfuerzos se han hecho para separar considerando un tiempo de adquisición no instantáneo, pero la corrección del mapa de campo y de R_2^* aún se realiza en el espacio de la imagen, donde el objeto no se encuentra en las posiciones correctas. En este trabajo presentamos un nuevo método para separar especies químicas en MRI. Ajustando los datos adquiridos a un modelo de señal que considera un tiempo de adquisición no instantáneo, el método propuesto es capaz de obtener de manera simultánea las especies químicas, la inhomogeneidad de campo y el mapa R_2^*. De esta forma se corrigen los artefactos causados por inhomogeneidades de campo y por desplazamiento químico en todas las variables estimadas. Imágenes 2D-GRE con diferentes tiempos de eco fueron adquiridas en la cabeza y el muslo. El ajuste de datos se realizó minimizando la norma l_2 entre la señal adquirida y modelada con un algoritmo de punto interior. Los resultados para los exámenes realizados muestran una excelente separación de agua y grasa con corrección R_2^*. Una mejor estimación en regiones donde existe sobreposición entre agua y grasa y buen desempeño en imágenes con bajo SNR sin aumentar el número de adquisiciones necesarias hacen de este método una buena alternativa a las técnicas comunes de separación de especies químicas.

Palabras Claves: MRI, Separación de especies químicas, Agua y Grasa, Inhomogeneidades de Campo, Mapa R_2^*.

1. INTRODUCTION

Separation of chemical species from magnetic resonance images is useful for assistance in patient diagnosis (Hussain et al., 2005). For example, discrimination of fat from water in the liver allows non-invasive fat quantification and fat fraction determination. The prominent signal brightness and spatial displacement of fat in some imaging studies can interfere with the diagnosis of pathologies, where reliable fat suppression proves to be difficult (Bley et al., 2010). Most fat-water separation techniques take advantage of the chemical shift between these species, which makes fat spins precess slower than water spins. This causes a displacement of the fat signal in the readout direction, and signal cancellation in out of phase images. Since the original two-point Dixon approach (Dixon, 1984), fat-water separation techniques have been considerably improved with new methods, such as three-point (Glover & Schneider, 1991) and multi-point Dixon (Glover, 1991), extended two-point Dixon (Skinner & Glover, 1997; Coombs et al., 1997; Hernando et al., 2008) and Iterative Decomposition of water and fat with Echo Asymmetry and Least-squares estimation (IDEAL) (Reeder et al., 2004, 2007), all of them successfully used for fat quantification (Kim et al., 2008). Multi-species separation is also possible with some of these approaches. Extended two-point Dixon and IDEAL incorporate the field inhomogeneity in their signal models, obtaining superior results compared to other techniques, which usually neglect this variable. Strong field inhomogeneities can distort species separation, so several phase unwrapping algorithms have been proposed to correct these distortions (Jenkinson, 2003; Hernando, Kellman, et al., 2010).

In order to obtain a better estimation of fat and water, the MR signal model should also take into account the effective transverse relaxation time (T_2^*) or rate ($R_2^* = 1/T_2^*$) of the species and the multi-peak spectrum model of fat. If the R_2^* for water and fat are not included in the reconstructed images, an erroneous estimation of the fat fraction can occur (Guiu & Aho, 2009; Hamilton et al., 2009; Bydder et al., 2008; Chebrolu et al., 2010). The R_2^* parameter can be incorporated in the signal model, yielding a more accurate calculation of the fat fraction (Hussain et al., 2005; Wood et al., 2005; Yu et al., 2007; Wang et al.,

2010; Chebrolu et al., 2010). Considering different decay rates for fat and water also improves the quantification of both species (Chebrolu et al., 2010). Additionally, the MR spectrum of fat ussually presents inter-subject variability (Hamilton et al., 2009; Machann et al., 2006). For example, the hepatic lipid concentration in the liver of different patients diagnosed with steatosis may differ significantly from that of healthy subjects (Machann et al., 2006). Traditionally, fat has been represented as a single peak 3.5 ppm away from the water peak. This allows a simple formulation of the signal, enabling an easily tractable framework for the theories used in fat suppression and saturation methods and Dixon-like methods. However, representing fat as a sum of several peaks located at different positions of the spectrum, weighed by the corresponding fraction of each peak, leads to a more accurate estimation of the fat fraction. It also allows the visualization of certain structures than can remain hidden when using a single peak approach (Hernando, Liang, & Kellman, 2010; Brodsky et al., 2010).

All the previous methods separate the species in image space, after the application of an inverse Fourier transform of k-space data. These schemes assume that the acquisition happens instantaneously at the echo time. This assumption produces some image distortions due to phase accumulation from off-resonance frequencies during the readout. This off-resonance deviation is caused by the combination of the species resonance frequency and the local field inhomogeneity. In some approaches, field inhomogeneity is corrected a posteriori (Eggers et al., 2011). Using a model based in a k-space formulation of the acquired signal that acknowledges the phase accumulation of off-resonance spins during the readout process leads to improvements, such as correction of chemical shift displacements or blurring. Brodsky et al. (Brodsky et al., 2008) used a variable time map, which successfully corrects chemical shift-related artifacts. A more complete signal model is presented in (Wang et al., 2010), where each pixel is modeled with a single R_2^* rate, generating a R_2^* map for the entire object. In both k-space decomposition methods the field and R_2^* maps are obtained in the image domain and then demodulated from the acquisitions. Unfortunately, image-space displacement caused by field inhomogeneity are difficult to correct using this approach. Additionally, when using low bandwidth acquisitions with

cartesian k-space trajectories where fat-water overlap may occur, a displaced estimation of the R_2^* decay is obtained, leading to an erroneous estimation of the species intensity.

In this work we propose a new method for Field Inhomogeneity, R_2^* and Species estimation using a variable Time map (FIRST). Unlike current methods, FIRST accounts for the phase accumulation due to field inhomogeneity and for the signal decay during the readout. Thus, it is able to correct the artifacts caused by chemical shift and field inhomogeneity. Moreover, the R_2^* map is calculated in the undisplaced positions. The estimation is achieved by minimizing the difference between the acquired signal and an accurate signal model of each k-space position. An interior-point algorithm was used to solve the minimization problem. Estimates for the unknowns are generated directly in image space. Similar to previous methods, it does not need specific echo time combinations, allowing the use of short echo time sequences, and a multi-peak signal model can be introduced for superior fat estimation.

2. THEORY

2.1. Review of IDEAL-like techniques

The IDEAL algorithm (Reeder et al., 2004, 2007) is an iterative method for achieving accurate separation of chemical species. As an extension of the multi-point Dixon technique, IDEAL can obtain separate images for M species with the acquisition of at least $M+1$ images at different echo times. The image quality will depend on the chosen echo times (Pineda et al., 2005), which are not restricted to specific phase shifts as in Dixon-like methods. Therefore, IDEAL is very useful for combining water-fat separation capabilities with short echo time (T_E) and pulse repetition time (T_R). The signal model used in IDEAL for one pixel at location $\mathbf{r}$ containing M species with chemical shifts Δf_m [Hz] ($m = 1, \ldots, M$) acquired during echo n at a discrete echo time t_n is the following,

$$s_n(\mathbf{r}) = \left(\sum_{m=1}^{M} \rho_m(\mathbf{r}) e^{i2\pi\Delta f_m t_n} \right) e^{i2\pi\psi(\mathbf{r})t_n}$$

with $\rho_m(\mathbf{r})$ the complex intensity of the mth species and $\psi(\mathbf{r})$ the local magnetic resonance offset (Hz). If $s_n^a(\mathbf{r})$ represents the acquired signal for all species in location $\mathbf{r}$, then the minimization functional of IDEAL for a set of pixels in position $\mathbf{r}$ is as follows,

$$\min_{\substack{\rho_m(\mathbf{r}) \in \mathbb{C} \\ \psi(\mathbf{r}) \in \mathbb{R}}} \left\| s_n^a(\mathbf{r}) - \sum_{m=1}^{M} \rho_m(\mathbf{r}) e^{i2\pi(\Delta f_m + \psi(\mathbf{r}))\cdot t_n} \right\|_2 .$$

This minimization is performed separately for each pixel and is implemented such that the current estimated field map is used to demodulate the acquired values. The resultant signal after demodulation is therefore

$$\hat{s}_n(\mathbf{r}) = s_n(\mathbf{r})\, e^{-i2\pi\psi(\mathbf{r})t_n} = \sum_{m=1}^{M} \rho_m(\mathbf{r})\, e^{i2\pi\Delta f_m t_n} .$$

After a linearization of the exponential term, a new estimate for the field map and species can be obtained with least squares, until the field map converges.

In the work of Brodsky et al. (Brodsky et al., 2008), the true time of the acquisition is given for each echo, allowing the correction of chemical shift-based displacement of species. If the time map is considered in the signal model, the inverse Fourier transform of $\hat{s}_n(\mathbf{r})$ is $\hat{S}_n(\mathbf{k})$ described by

$$\hat{S}_n(\mathbf{k}) = \sum_{m=1}^{M} R_m(\mathbf{k})\, e^{i2\pi\Delta f_m(t_n+\tau_{\mathbf{k},n})}$$

where $R_m(\mathbf{k})$ are the Fourier transform of the species, t_n is the nominal echo time and $\tau_{\mathbf{k},n}$ is the relative time between the acquisition of sample point $\mathbf{k}$ and the center of k-space. The comparison of the assumed trajectories for fixed and variable time maps in cartesian acquisitions is shown in figure 2.1. Using a similar decomposition method as in conventional IDEAL, the Fourier values for each species are obtained, leading to non-shifted estimates of fat and water. Nevertheless, the field map is demodulated in image space, as if it were acquired with a fixed time map. For this reason, displacements caused by field inhomogeneity are not corrected, whose implications are described later. All these methods are denoted as image-space decomposition algorithms, since they demodulate the field map in image-space. Image-space methods consider a fixed time map as an approximation to the true time map, which is not constant.

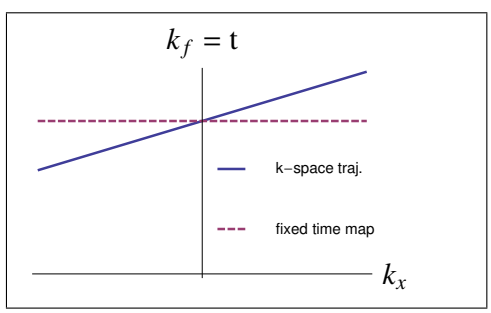

FIGURE 2.1. Comparison between the actual k-space trajectory and the assumed trajectory for fixed time map (image space) methods when using a cartesian acquisition. The solid line shows the k_x-k_f trajectory, and the dashed line is the approximation for image space methods. The k_f value at $k_x = 0$ is the echo time of the acquisition. As the acquisition bandwidth increases, the slope of the solid line decreases. The horizontal line corresponds to an infinite bandwidth acquisition.

2.2. FIRST signal model

Considering a k-space trajectory given by $k(t)$, the estimated MR signal for an object containing M different species is given by

$$S^e(t) = \sum_{m=1}^{M} \int \rho_m(\mathbf{r}) e^{-i2\pi[\mathbf{r}\cdot k(t)+(\Delta f_m+\psi(\mathbf{r}))\cdot t]}\, d\mathbf{r} \ .$$

This signal model takes into account a variable time map for the chemical shift of each species and the field map intensities for each position. For a single species m, the discrete version of the estimated signal $S^e_m(t)$ is given by

$$S^e_{mq} = \sum_{\mathbf{r}} \rho_{m,\mathbf{r}} e^{-i2\pi(\Delta f_m+\psi_{\mathbf{r}})\cdot q}\, e^{-i2\pi \mathbf{r}\, k_q}$$

where $\mathbf{r}$ is the discrete position of spin densities and q is the time at which sample k_q was acquired. The purpose is to adjust the unknown variables of the estimated model ($\boldsymbol{\rho}_m$ and $\boldsymbol{\psi}$) to the values of the acquired signal. If S^a_q is the acquired signal for all species at a specific time q, the reconstruction functional is

$$\min_{\substack{\boldsymbol{\rho}_m \in \mathbb{C}^N \\ \boldsymbol{\psi} \in \mathbb{R}^N}} \left\| S^a_q - \sum_{m=1}^{M} \sum_{\mathbf{r}} \rho_{m,\mathbf{r}} e^{-i2\pi(\Delta f_m+\psi_{\mathbf{r}})\cdot q}\, e^{-i2\pi \mathbf{r}\, k_q} \right\|_2 . \tag{2.1}$$

In this minimization there are $2M+1$ unknowns of length N (M is the number of species and N the number of acquired points). Each acquisition adds $2N$ equations to the system. It is necessary to acquire $M+1$ times to have a complete set of equations and unknowns. Therefore, our method does not increase the amount of data needed for species separation when compared to similar decomposition methods. The objective function is similar to the one in (Hernando, Kellman, et al., 2010), with the difference that in this model a variable time map is introduced. In the following section, we will describe a more complete signal model that takes into account the T_2^* decay of the signal. In the discussion we will refer to multi-peak fat spectrum. The extension for 2D cartesian acquisitions can be found in

appendix A.

2.3. T_2^* decay

The previous formulations do not consider the T_2^*decay of the MR signal. Correcting the species intensities from their T_2^* decay produces better results, specially for those species with short T_2^* times (Chebrolu et al., 2010). In (Yu et al., 2007), the signal model assumes the same T_2^* value for every species if they coexist in a single voxel. For that approach, they introduced a new notation where the field map is complex and denoted by $\tilde{\psi}(\mathbf{r}) = \psi(\mathbf{r}) + i\, R_2^*(\mathbf{r})/2\pi$. For image-space decomposition algorithms, the complex field map is demodulated from the acquired signal in image space. Considering a fixed time map for the complex field map may lead to some distortions. For example, if cartesian imaging is used, species estimates are erroneously R_2^*-rectified in fat-water overlapping regions. This case can be typically found in low-bandwidth acquisitions. Similar examples can be encountered for other trajectories. Moreover, acquisitions with different bandwidths (and different off-resonance artifacts) would produce severely erroneous field and R_2^* maps, that will affect the separation of species when demodulating the maps in image space before the separation process.

When considering a variable time map, the signal decay at each sampling time can be corrected, which is not possible to do if a fixed time map for the complex field map is considered. In our model we will consider a single R_2^* parameter for all species within a pixel. It is important to note that the MR signal depends on the acquisition time, so the exponential decay must depend on the time map t rather than T_E only. Then the discrete minimization functional is

$$\min_{\substack{\boldsymbol{\rho}_m \in \mathbb{C}^N \\ \tilde{\boldsymbol{\psi}} \in \mathbb{C}^N}} \left\| S_q^a - \sum_{m=1}^{M} \sum_{\mathbf{r}} \rho_{m,\mathbf{r}} \cdot e^{-i2\pi(\Delta f_m + \tilde{\psi}_{\mathbf{r}})\cdot q} \cdot e^{-i2\pi \mathbf{r}\, k_{\mathbf{r}}} \right\|_2 .$$

The minimization of this functional yields $\rho_m(x)$, $\psi(x)$ and $R_2^*(x)$ in their non-displaced positions. In this case, $2M + 2$ acquisitions are needed to obtain the estimates. In our formulation, the $\tilde{\psi}$ term is multiplied by the time map of the acquisition, so the signal decay during the readout is considered.

3. METHODS

3.1. MRI Acquisitions

A conventional 2D gradient echo sequence with cartesian trajectories was performed in the thigh and brain of two healthy subjects. Institutional Review Board approval and informed consent were obtained from volunteers prior to imaging. All images were obtained using a Philips Intera 1.5T scanner (Philips Healthcare, Best, The Netherlands). For thigh imaging, a four element body coil was used, and four acquisitions were obtained with the following parameters: matrix size 256×256, TE = 4.6, 4.8, 6.2, 7.5 ms, Flip Angle (FA) = 25°, slice thickness = 10 mm, TR = 150 ms, Field Of View (FOV) = 18 cm with sampling bandwidth of $\pm$ 13.8 kHz (217 Hz/pixel), scan time = 152 seconds. For brain imaging, a quadrature head coil was used, with the same sequence parameters expect for FOV = 25.6 cm. TR and TE were arbitrarily chosen to achieve similar signal intensities from fat and water, while maintaining a short scan time. Automatic shimming procedures were not performed in any of the scans. No windowing or other filtering approaches were applied to the acquired data in order to achieve maximal resolution. For each data set, complex echo images were processed to obtain estimates of fat and water with FIRST and IDEAL algorithms. The water-fat frequency shift was assumed to be -3.5 ppm, or -217.1 Hz at 1.5T. Magnitude images for fat, water and in-phase combination (water plus fat) were generated in addition to field and R_2^* maps.

3.2. IDEAL algorithm

An implementation of the T_2^*-IDEAL algorithm (Yu et al., 2007) was written in MATLAB 7.4 (The MathWorks Inc., Natick, MA, USA). We first performed a standard IDEAL decomposition (Reeder et al., 2004). The resulting species and field map were used as a starting point for calculating the complex field map and the corrected species for T_2^*-IDEAL, as suggested in (Yu et al., 2007). The ranges for field inhomogeneity and R_2^* were set to -150 to 150 Hz and 0 to 350 s^{-1} respectively. Even though field inhomogeneity is usually set in the range $[-\Delta f_{\text{fat}}/2, \Delta f_{\text{fat}}/2]$ (Hernando, Kellman, et al., 2010),

we decided to broaden these limits to avoid phase wraps. For each pixel, an update of less than 10^{-2} Hz for the field map and $10^{-4}\ s^{-1}$ for R_2^* were used as the stopping condition. A maximum of 200 iterations were executed for both IDEAL and T_2^*-IDEAL if these tolerances were not reached. Before calculating the final estimate of species, the field map was filtered with a gaussian filter of size 3×3 and $\sigma = 1.5$ in order to achieve better water-fat separation. The processing time for a set of four acquisitions of size 256×256 pixels was 9 minutes. From now on, we will refer to T_2^*-IDEAL simply as IDEAL.

3.3. FIRST algorithm

Our proposed technique requires an optimization algorithm suitable for a non-linear objective function with linear constraints. We used the interior-point algorithm (Karmarkar, 1984; Byrd et al., 1999) available in the `fmincon` function of MATLAB's Optimization Toolbox. The interior-point method was chosen for being stable and faster than other available options, such as trust-region reflective, active set and SQP. Upper and lower bounds are provided for all variables. For each pixel of the species, a maximum absolute value is defined as 1.5 times the maximum absolute value available in all acquisitions. This maximum value is used as the upper bound for the real and imaginary parts of every species. The negative of the maximum value is used for the lower bound. The ranges for field inhomogeneity and R_2^* were the same as in IDEAL. There are no additional constrains for the variables, although they could be used to assure certain smoothness of the field and R_2^* map.

Our final implementation consisted of two steps. The first step consists in estimating the species and the field map without considering R_2^* decay. In the second step we re-estimate the species and the field map but now calculating a R_2^* map (with a single R_2^* value per pixel). The estimates for the species and field map are used as the starting point of the second step. A flowchart of the optimization process is shown in figure 3.1. Our minimization problem is a non-linear and non-convex problem, with multiple local minima. The global minimum can be reached through multiple solutions, due to the complex exponential terms of the MR signal model described in the objective function. We

will discuss this later. Bounds for all variables were provided, creating a convex feasible set. Even for this complicated objective function, the algorithm proved to be useful at estimating the unknown variables. Explicitly calculated gradients were supplied for speed improvements, which can be found in Appendix B. The objective value and the gradients of the objective function were calculated with an auxiliary function written in C and compiled with Microsoft Visual C++ 2010. Three different stopping criteria were used for each step of the algorithm: a step size norm lower than 10^{-9} or a maximum of 280 iterations or an objective function lower than 10^{-7}, whichever was reached first. These values were chosen experimentally and applied for both steps of the estimation process. The processing time for a set of four acquisitions of size 256×256 pixels was 71 minutes.

To speed up the convergence of IDEAL and FIRST, an initial estimate for the R_2^* map was generated. The initial value of R_2^* for each pixel was calculated by fitting a single exponential function to the absolute values of each acquisition. Values outside the 0 to 350 s^{-1} range were saturated. These are within the normal range even for subjects with very high iron deposition (Gatehouse & Bydder, 2003; Wood et al., 2005; Wang et al., 2010). After calculating the value for each pixel in the image, a mask was applied in order to eliminate the values outside the object. Finally, the result was smoothed with a gaussian filter of size 5×5 and $\sigma = 1$. This procedure only adds 34.4 seconds. All computations were performed in a computer with an Intel i7 processor (4 cores, 3.4 GHz, 64-bit) with 8 GB of RAM.

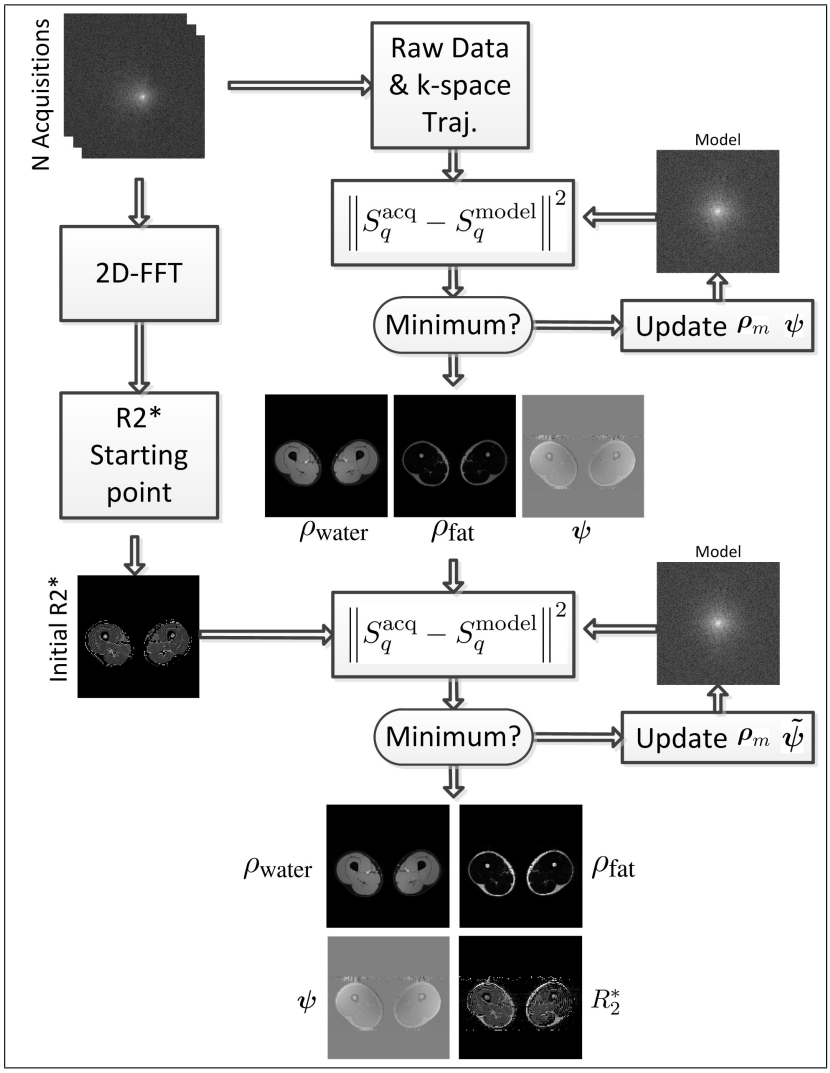

FIGURE 3.1. Flowchart of our implementation for solving the optimization problem. It considers a two-step minimization. The first step consists of estimating the complex value of the chemical species (ρ_{water}, ρ_{fat}) and field map (ψ). When these variables are calculated, they are used as an input for the second step, which calculates the R_2^* and field maps and re-estimates species. We used a starting point for R_2^* based on an exponential fitting of the signal decay.

4. RESULTS

The results for FIRST and IDEAL when processing gradient echo images of the thigh are shown in Figs. 4.1 to 4.3. Images for absolute values of water, fat, water plus fat, field inhomogeneity and R_2^* are presented. Water plus fat images were obtained by adding the complex values of water and fat, followed by taking the absolute value of the result. FIRST provides better results for the species in regions with water-fat overlap, mainly because the R_2^* decay is well positioned compared to the map generated with IDEAL. The voxel size for this acquisition was 4.94 mm^3, which notably increases the noise level of the input images. This makes exponential fitting for R_2^* estimation specially difficult. Although a smoothing for R_2^* is not specified in the original literature of IDEAL, this step is included to address the high variance present in the R_2^* map, which leads to noisy species estimates. Brain images can be found in Figs. 4.4 to 4.6. Brain acquisitions at the orbits level are particularly difficult in water-fat separation procedures due to the high field inhomogeneities caused by the air present in the sinus, as Fig. 4.5 shows. High field inhomogeneities could cause high frequency fat-water swapping, degrading the quality of the species estimates. Nevertheless, high frequency field variations were not observed throughout the image when using both methods. These variations are attenuated in IDEAL because the field map is smoothed in the final step, which yields a less defined field map. It is important to note that the field inhomogeneity and R_2^* estimates of FIRST remain very close to the starting point in areas where the object is close to zero. In practice, estimates of these variables with low noise backgrounds improve the visualization of the generated maps. Low changes in the maps can be understood by looking at the gradients of the objective function (Appendix B), where the change of the estimates of field inhomogeneity and R_2^* are directly weighed by the object intensities. Image indicators for a selected region in each set are shown in Table 4.1. An approximation of the SNR (apparent SNR) was calculated as the quotient between the mean of the absolute value of the region of interest and the standard deviation of the background. Good estimates for R_2^* maps were obtained with FIRST and IDEAL considering only four echoes.

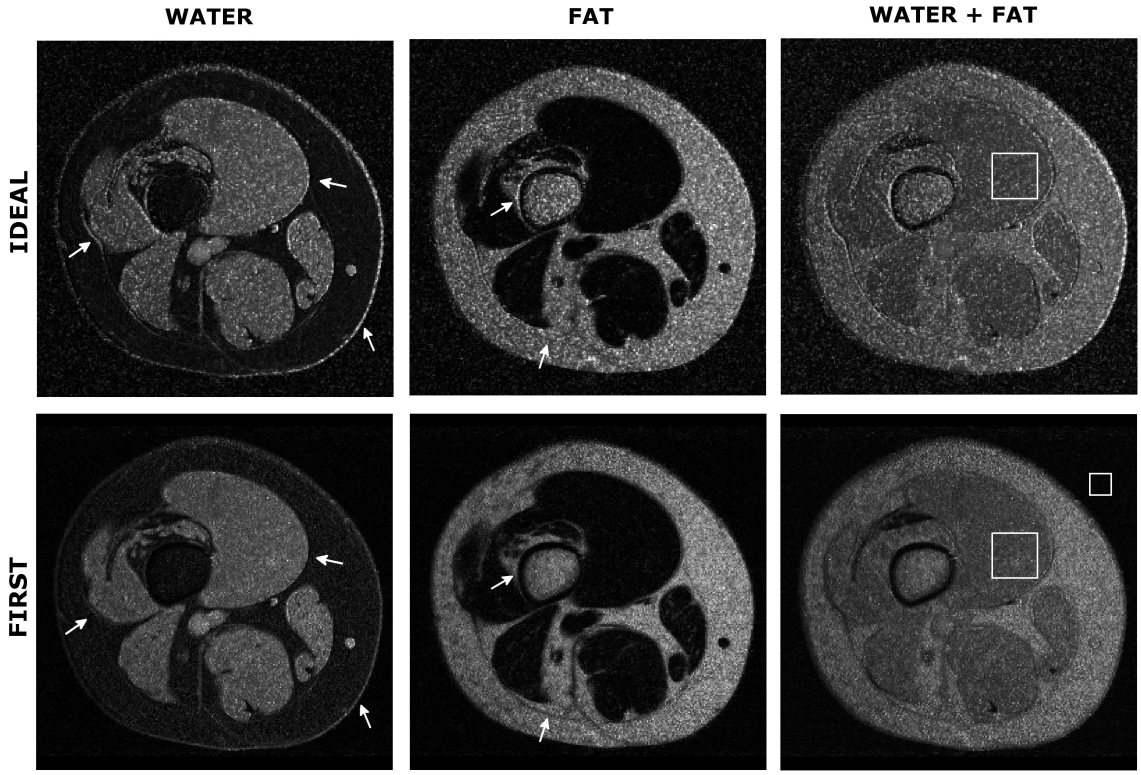

FIGURE 4.1. Absolute values of imaging estimates of water, fat and sum of both components for the thigh. The upper and lower rows show the results for IDEAL and FIRST, respectively. The arrows show areas where notable differences are observed, like signal accentuation in borders. For example, in the water component estimated with IDEAL, an intensified signal band can be observed. Also, due to the lower noise of FIRST estimates, more details can be appreciated in fat images (lower arrow). The region in the white rectangle was used to obtain the image indicators shown in Table 4.1. All images are shown with the same intensity scale.

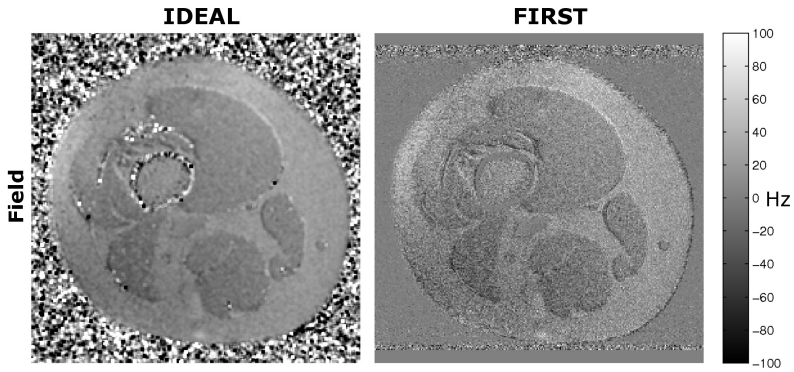

FIGURE 4.2. For the thigh, left and right images show the calculated field inhomogeneity map with IDEAL and FIRST, respectively. The field map calculated with IDEAL was smoothed with a 5×5 and $\sigma = 1.5$ gaussian filter. Similar intensities are observed for both methods, validating our technique for the measurement of the field map, although our method provides a more detailed field map. A small advantage FIRST is given by the small changes of the complex field map where the signal level is low. This results in reduced background noise, improving the visibility of the results.

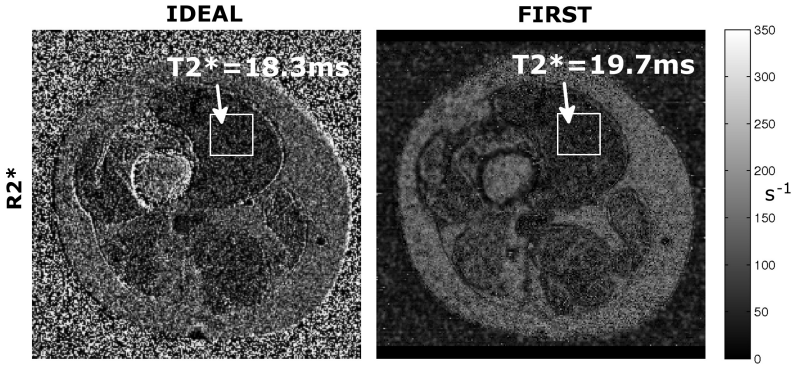

FIGURE 4.3. For the thigh, left and right columns show the calculated R_2^* with IDEAL and FIRST, respectively. The R_2^* map of IDEAL was smoothed with a 5×5 and $\sigma = 0.5$ gaussian filter, as explained in section 3.3. The shown T_2^* values were calculated as the mean of a 22×22 rectangle. In this case we can see a lower value of T_2^* with IDEAL, yielding higher signal intensities when compared to FIRST. A smoother map is obtained with FIRST, avoiding peak values which may lead to incorrect estimation of R_2^*.

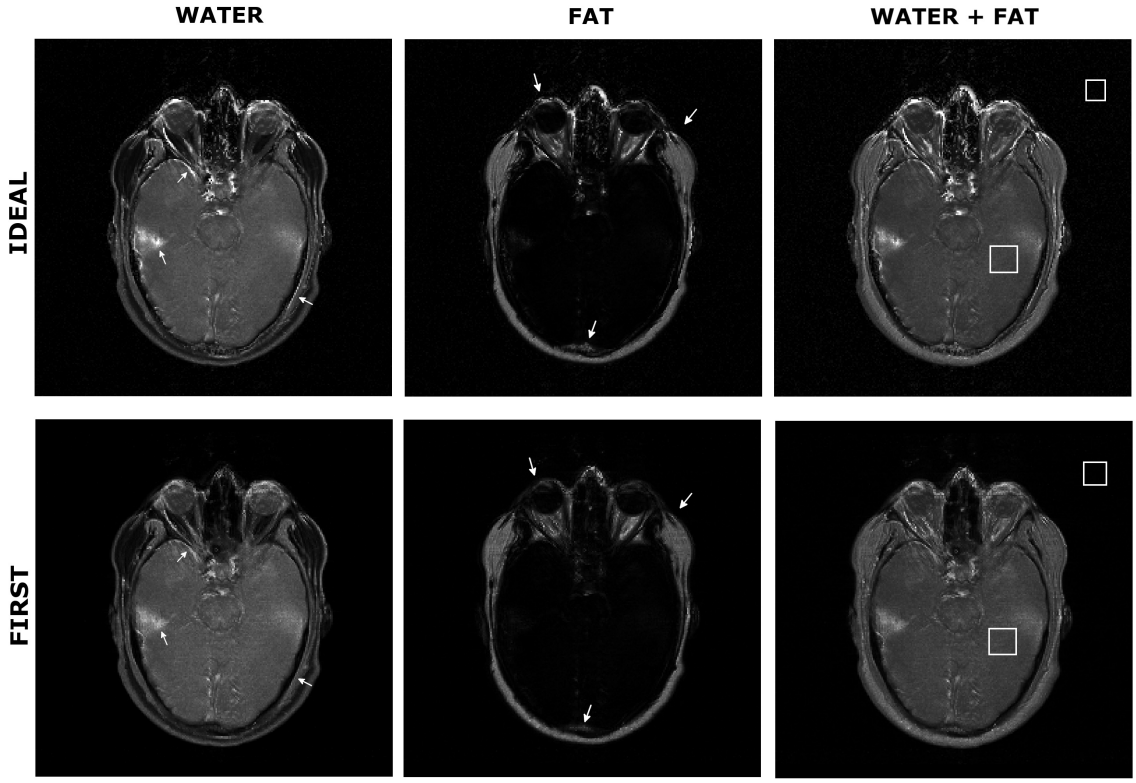

FIGURE 4.4. Absolute values of imaging estimates of water, fat and sum of both components for the brain. The upper and lower rows show the results for IDEAL and FIRST, respectively. Lower noise is observed for both separations methods, due to the larger voxel size of the input images. Higher signal intensities are observed for the water and fat estimates of IDEAL, shown by the arrows. The rectangle shows the area used for obtaining the image indicators of Table 4.1. All images are shown with the same intensity scale.

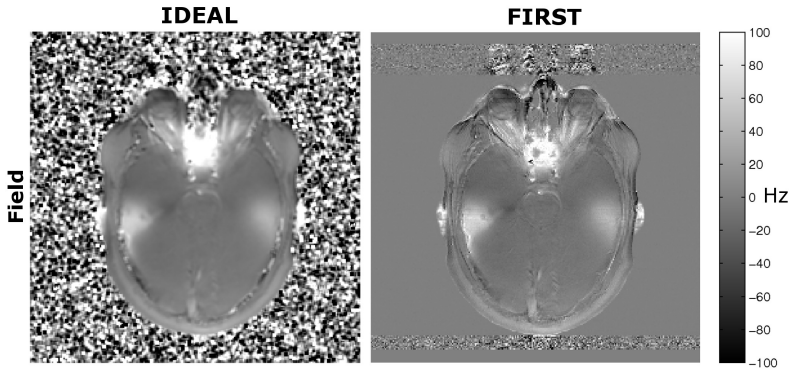

FIGURE 4.5. For brain imaging, calculated field inhomogeneity map with IDEAL and FIRST. The field map calculated with IDEAL was smoothed with a 5×5 and $\sigma = 1.5$ gaussian filter. Moderate phase wrap occurs for both algorithms near the sinus, although high field inhomogeneities are present.

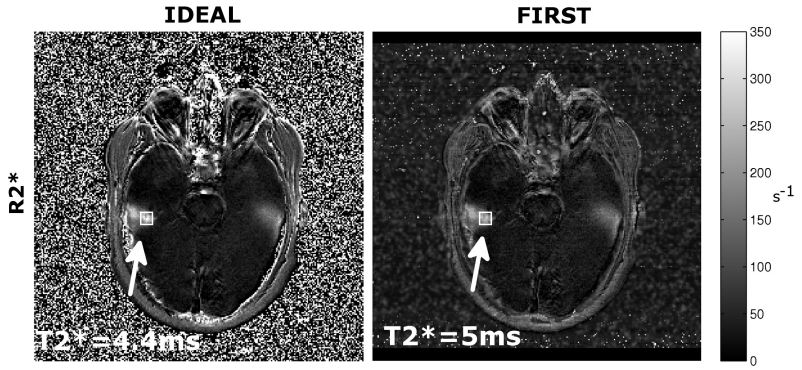

FIGURE 4.6. For brain imaging, calculated R_2^* with IDEAL and FIRST. The R_2^* maps were not smoothed except for the starting point, as explained in section 3.3. The shown T_2^* values were calculated as the mean of a 22×22 rectangle. Similar to thigh imaging, IDEAL estimates a shorter T_2^* time when compared to FIRST, which yields higher intensity values. This can cause over-estimation of the fat fraction.

		IDEAL	FIRST
Thigh	μ_{water}	0.35	0.34
	μ_{fat}	0.033	0.033
	$\text{ASNR}_{\text{w+f}}$	11.6	21.8
	T_2^* [ms]	17.58	18.05
	B_0 [Hz]	9.82	9.05
Brain	μ_{water}	1.93	1.94
	μ_{fat}	0.07	0.07
	$\text{ASNR}_{\text{w+f}}$	51.0	134.0
	T_2^* [ms]	23.02	23.84
	B_0 [Hz]	6.96	6.91

TABLE 4.1. Image indicators for different sets and processing algorithms. The selected signal regions are shown in Figs. 4.1 and 4.4 for thigh and brain. The apparent signal-to-noise ratio (ASNR) was calculated as the fraction between the mean value of the selected region and the standard deviation of the background signal. Similar values for the mean intensities of water (μ_{water}), fat (μ_{fat}), field map (B_0) and $R_2^*$with FIRST and IDEAL were found in both sets, validating our method for species separation. For both sets there is an over-estimation of the R_2^* map for IDEAL, which might result in higher intensity values. Because the selected rectangle contains mostly water, there is no significant difference in the intensity values of the species for both methods. Better noise performance (higher ASNR) is observed for FIRST, making it a good alternative for low SNR input images.

5. DISCUSSION

Our frequency space-based approach calculates simultaneously estimates of species, field inhomogeneity and R_2^* maps. By calculating the field and R_2^* maps concurrently with the species, we obtain non-shifted estimates of the first two. Additionally, the proposed method corrects image-space displacement of species due to chemical shift and field inhomogeneity (Figs. 4.1 to 4.6). As shown in the results, this technique achieves accurate and reliable water-fat separation. Estimates with less noise are obtained with FIRST, providing better visualization of the images. Structures that may remain hidden are easily distinguished with our method. Besides, a smoother R_2^* map is generated with FIRST, avoiding peak intensities which may lead to erroneous calculation of this parameter.

We have shown that the water signal calculated with image space-based algorithms is erroneously intensified in areas where there is water-fat overlap due to chemical shift artifacts. Techniques using variable time maps with pre-separation R_2^*-correction also suffer from this problem, because the R_2^* map is estimated before off-resonance correction, obtaining a shifted estimate of the R_2^* map. This artifact is repaired when adopting a simultaneous estimation scheme like the one we have presented. In the case where different bandwidths are needed for each echo, each acquisition will suffer from different off-resonance artifacts in image space, leading to erroneous estimation of the field inhomogeneity and R_2^* maps if these are calculated from the input images. Although it was not evaluated, our method would allow different bandwidth acquisitions, without sacrificing accuracy in the estimation of the field and R_2^* maps.

As has been already noted, the water-fat separation problem has multiple solutions if the field inhomogeneity is not bounded to an adequate range. This range depends on the resonant frequencies of the species (Dixon, 1984; Skinner & Glover, 1997; Reeder et al., 2004; Hernando, Liang, & Kellman, 2010). Therefore, the optimization problem proposed in Eq. 2.1 is non-convex. A priori, interior-point algorithms are not well-suited for non-convex problems, where several local minima coexist (Karmarkar, 1984; Byrd et al., 1999), and the global minima can be obtained with multiple solutions. In our case,

the algorithm is capable of generating a reasonable solution due to the chosen starting points and the boundaries for the unknown variables. In fact, using only bounds and no other type of restrictions simplify significantly the calculation of the logarithmic barrier of the interior-point method. For FIRST, the starting point of species and field map is chosen to be zero. For the R_2^* map, an exponential fitting of the magnitude values of the acquired images is used as initial value, which results in faster convergence to the solution. Because of the characteristics of the chosen algorithm, it is important to broaden the bounds of the variables, because interior-point method solutions never lie totally in the specified boundaries (Nocedal & Wright, 1999).

Our final implementation for solving the minimization problem consisted of two steps. Empirically, we found that separating into two steps was faster than solving the whole problem at once. The objective function value obtained when solving the minimization problem in a single step was 10% higher than the value obtained with two steps for equal processing time.

An important problem in species separation techniques is water-fat swap. Different heuristics can be included to avoid rapidly changing field map estimates. Given our theoretical framework, it is convenient to include field map smoothness restrictions in the optimization problem. Several smoothness conditions have been proposed to address this issue (Hernando, Liang, & Kellman, 2010; Samsonov et al., 2008; Funai et al., 2008). On the other hand, some image-space techniques have been proposed for species separation in the presence of high field inhomogeneities, such as region growing methods for field map estimation (Yu et al., 2005).

FIRST was demonstrated with data sets with traditional cartesian spin warp, but our theoretical framework allows any k-space trajectory, and even different trajectories for each echo. A specific implementation that takes advantage of the time map characteristics of cartesian spin warp was implemented, and a more general computational solver for any 2D sequence is being explored as future work. With a general 2D solver, radial, spiral and other trajectories can be used in combination with our method.

Multi-peak fat spectrum modeling has proved to be useful for fat separation techniques. A multi-peak model can be easily incorporated to our approach. The amplitude coefficients and peak frequencies of the fat spectrum can be calculated on a patient-specific basis through spectroscopy or other method.

The main limitations of this work can be summarized in two. The first one is computational time for separation. For data sets of the same size, FIRST takes 71 minutes, much longer than the 9 minutes of T_2^*-IDEAL. Choosing a more suitable optimization algorithm for this kind of non-linear problem is being studied as an option. The Variable Projection (VARPRO) method (Golub & Pereyra, 1972, 2003) has been previously used in MRI and MR spectroscopy for species separation purposes with promising results (Veen et al., 1988; Hernando et al., 2008). This approach will be studied for the application to the proposed theory. The second limitation is that a single R_2^* value is assumed for both species, which leads to sub-optimal fat quantification (Chebrolu et al., 2010). Anyhow, this issue can be addressed with our proposed scheme, without increasing the number of variables required for solving the fat-water separation problem. We have adopted a solution that in a first step the field map is calculated along with the species, leaving a set of N redundant equations. If in the second step the field map from the previous step is considered correct, therefore calculating only the R_2^* map and the species, we leave N free equations. This set of free equations can be used for calculating independent R_2^* values for fat and water. An approach for calculating two different R_2^* values with IDEAL has been presented recently in (Janiczek et al., 2011). This feature is being considered for future implementations.

6. CONCLUSION

A method for simultaneously estimating chemical species, field inhomogeneity and R_2^* maps without off-resonance displacements was presented, obtaining excellent results for different examinations. This method is specially well suited for low bandwidth acquisitions. Although we implemented the method only for traditional cartesian spin warp acquisitions, the theoretical framework permits the usage of any trajectory.

7. FUTURE WORK

The main contribution of the presented work consists in proposing a complete signal model for the species separation problem in MRI. For an object containing different species, the acquired signal is modeled entirely in k-space. This allows to take into account the phase accumulation of spins due to chemical shift and field inhomogeneity during the readout. In addition, the signal decay during the readout due to the R_2^* parameter is also considered. The benefits of this consideration are not very clear, and could be reflected more clearly when using other types of k-space trajectories. Considering the readout time for field inhomogeneity and R_2^* have not been introduced in previous species separation approaches.

The next step for improving this technique is to develop a 2D solver, in order to use any kind of k-space trajectories. Most probably, a MATLAB implementation for a complete 2D reconstruction is not going to sufficiently fast, so lower level languages such as C or C++ should be considered. The gradients of the objective function have already been programmed in C, decreasing the processing time notably. Alongside, restrictions for smoothness of the field or R_2^* maps can be included in the optimization problem formulation. Different references for this subject have been outlined in the previous chapter of this document. One possibility for reducing the processing time can be derived from the signal model itself. The complexity of the optimization lies in the non-linearity of the exponential term. If the complex field map (field inhomogeneity and R_2^*) is known, then the species variables can be estimated by least-squares calculation. Given the species estimates, the complex field map can be re-calculated. Separating the optimization in this two-step loop yields a non-linear optimization problem of only $2N$ variables, instead of the $2N * (M + 1)$ variables of the straightforward approach. The remaining $2NM$ species variables are calculated almost instantly with least-squares, reducing the complexity of the optimization problem. The two steps can be repeated until convergence is reached.

In summary, the main focus for future work should be put in lowering the processing time and developing a true 2D solver for more general acquisitions. These are the main constraints for a wider adoption of this technique.

References

Bley, T., Wieben, O., François, C. J., Brittain, J. H., & Reeder, S. B. (2010). Fat and water magnetic resonance imaging. *J Magn Reson Imaging*, *31*(1), 4–18.

Brodsky, E. K., Chebrolu, V. V., Block, W. F., & Reeder, S. B. (2010). Frequency response of multipoint chemical shift-based spectral decomposition. *J Magn Reson Imaging*, *32*(4), 943–952.

Brodsky, E. K., Holmes, J. H., Yu, H., & Reeder, S. B. (2008). Generalized k-space decomposition with chemical shift correction for non-Cartesian water-fat imaging. *Magn Reson Med*, *59*(5), 1151–1164.

Bydder, M., Yokoo, T., Hamilton, G., Middleton, M. S., Chavez, A. D., Schwimmer, J. B., et al. (2008). Relaxation effects in the quantification of fat using gradient echo imaging. *Magn Reson Imaging*, *26*(3), 347–359.

Byrd, R. H., Hribar, M. E., & Nocedal, J. (1999). An Interior Point Algorithm for Large-Scale Nonlinear Programming. *SIAM J Optim*, *9*(4), 877–900.

Chebrolu, V. V., Hines, C. D. G., Yu, H., Pineda, A. R., Shimakawa, A., McKenzie, C. a., et al. (2010). Independent estimation of T2* for water and fat for improved accuracy of fat quantification. *Magn Reson Med*, *63*(4), 849–857.

Coombs, B. D., Szumowski, J., & Coshow, W. (1997). Two-point Dixon technique for water-fat signal decomposition with B0 inhomogeneity correction. *Magn Reson Med*, *38*(6), 884–889.

Dixon, W. T. (1984). Simple proton spectroscopic imaging. *Radiology*, *153*(1), 189–194.

Eggers, H., Boernert, P., & Koken, P. (2011). Spiral water-fat imaging with integrated off-resonance correction on a clinical scanner. In *Proc intl soc mag reson med* (Vol. 19, pp. 752–752).

Funai, A. K., Fessler, J. A., Yeo, D. T. B., Olafsson, V. T., & Noll, D. C. (2008). Regularized field map estimation in MRI. *IEEE Trans Med Imaging*, *27*(10), 1484–1494.

Gatehouse, P., & Bydder, G. (2003). Magnetic Resonance Imaging of Short T2 Components in Tissue. *Clin Radiol*, *58*(1), 1–19.

Glover, G. H. (1991). Multipoint Dixon Technique for Water and Fat Proton and susceptibility Imaging. *J Magn Reson Imaging*, *1*(5), 512–530.

Glover, G. H., & Schneider, E. (1991). Three-point dixon technique for true water/fat decomposition with B0 inhomogeneity correction. *Magn Reson Med*, *18*(2), 371–383.

Golub, G., & Pereyra, V. (1972). The differentiation of pseudoinverses and nonlinear least squares problems whose variables separate. *SIAM J Numer Anal*, *10*(2), 413–432.

Golub, G., & Pereyra, V. (2003). Separable nonlinear least squares: the variable projection method and its applications. *Inverse Problems*, *19*(2), R1–R26.

Guiu, B., & Aho, S. (2009). Quantification of Liver Fat Content : Comparison of Triple-Echo and in Vivo Proton MR Spectroscopy 1. *Clinical Research*, *250*(1), 95–102.

Hamilton, G., Middleton, M. S., Bydder, M., Yokoo, T., Schwimmer, J. B., Kono, Y., et al. (2009). Effect of PRESS and STEAM sequences on magnetic resonance spectroscopic liver fat quantification. *J Magn Reson Imaging*, *30*(1), 145–152.

Hernando, D., Haldar, J. P., Sutton, B. P., Ma, J., Kellman, P., & Liang, Z.-P. (2008). Joint estimation of water/fat images and field inhomogeneity map. *Magn Reson Med*, *59*(3), 571–580.

Hernando, D., Kellman, P., Haldar, J. P., & Liang, Z.-P. (2010). Robust water/fat separation in the presence of large field inhomogeneities using a graph cut algorithm. *Magn Reson Med*, *63*(1), 79–90.

Hernando, D., Liang, Z.-P., & Kellman, P. (2010). Chemical shift-based water/fat separation: A comparison of signal models. *Magn Reson Med*, *64*(3), 811–822.

Hussain, H. K., Chenevert, T. L., Londy, F. J., Gulani, V., Swanson, S. D., McKenna, B. J., et al. (2005). Hepatic fat fraction: MR imaging for quantitative measurement and display–early experience. *Radiology*, *237*(3), 1048–1055.

Janiczek, R. L., Gambarota, G., Sinclair, C. D. J., Yousry, T. a., Thornton, J. S., Golay, X., et al. (2011). Simultaneous T2 and lipid quantitation using IDEAL-CPMG. *Magn Reson Med*, *65*(Early View).

Jenkinson, M. (2003). Fast, automated, N-dimensional phase-unwrapping algorithm. *Magn Reson Med*, *49*, 193–197.

Karmarkar, N. (1984). A new polynomial-time algorithm for linear programming. *Combinatorica*, *4*(4), 373–395.

Kim, H., Taksali, S. E., Dufour, S., Befroy, D., Goodman, T. R., Petersen, K. F., et al. (2008). Comparative MR study of hepatic fat quantification using single-voxel

proton spectroscopy, two-point dixon and three-point IDEAL. *Magn Reson Med*, *59*, 521–527.

Machann, J., Thamer, C., Schnoedt, B., Stefan, N., Haring, H.-U., Claussen, C. D., et al. (2006). Hepatic lipid accumulation in healthy subjects: a comparative study using spectral fat-selective MRI and volume-localized 1H-MR spectroscopy. *Magn Reson Med*, *55*(4), 913–917.

Nocedal, J., & Wright, S. J. (1999). *Numerical optimization* (P. Glynn & S. M. Robinson, Eds.). New York: Springer-Verlag.

Pineda, A. R., Reeder, S. B., Wen, Z., & Pelc, N. J. (2005). Cramér-Rao bounds for three-point decomposition of water and fat. *Magn Reson Med*, *54*(3), 625–635.

Reeder, S. B., McKenzie, C. A., Pineda, A. R., Yu, H., Shimakawa, A., Brau, A. C., et al. (2007). Water-fat separation with IDEAL gradient-echo imaging. *Magn Reson Med*, *25*, 644–652.

Reeder, S. B., Wen, Z., Yu, H., Pineda, A. R., Gold, G. E., Markl, M., et al. (2004). Multicoil Dixon chemical species separation with an iterative least-squares estimation method. *Magn Reson Med*, *51*, 35–45.

Samsonov, A., Fessler, J., & Huh, W. (2008). Water-Fat Decomposition with Regularized field map. *Proc Intl Soc Mag Reson Med*, *16*, 1382.

Skinner, T. E., & Glover, G. H. (1997). An Extended Two-Point Dixon Algorithm for Calculating Separate Water, Fat, and B0 Images. *Magn Reson Med*, *37*(4), 628–630.

Veen, J. W. van der, Beer, R. de, Luyten, P. R., & Ormondt, D. van. (1988). Accurate quantification of in vivo 31P NMR signals using the variable projection method and prior knowledge. *Magn Reson Med*, *6*(1), 92–98.

Wang, K., Yu, H., Brittain, J. H., Reeder, S. B., & Du, J. (2010). k-space water-fat decomposition with T2* estimation and multifrequency fat spectrum modeling for ultrashort echo time imaging. *J Magn Reson Imaging*, *31*(4), 1027–1037.

Wood, J. C., Enriquez, C., Ghugre, N., Tyzka, J. M., Carson, S., Nelson, M. D., et al. (2005). MRI R2 and R2* mapping accurately estimates hepatic iron concentration in transfusion-dependent thalassemia and sickle cell disease patients. *Blood*, *106*(4), 1460–1465.

Yu, H., McKenzie, C. A., Shimakawa, A., Vu, A. T., Brau, A. C., Beatty, P. J., et al. (2007). Multiecho reconstruction for simultaneous water-fat decomposition and T2* estimation. *J Magn Reson Imaging*, *26*, 1153–1161.

Yu, H., Reeder, S. B., Shimakawa, A., Brittain, J. H., & Pelc, N. J. (2005). Field map estimation with a region growing scheme for iterative 3-point water-fat decomposition. *Magn Reson Med*, *54*(4), 1032–9.

Appendix

APPENDIX A. FORMULATION FOR 2D CARTESIAN ACQUISITIONS

Extending the formulation of section 2.2 to a 2D acquisition, the signal for one specific echo time can be described as

$$\begin{aligned} S(k_x, k_y) &= \sum_{m=1}^{M} \iint \rho_m(x,y) e^{-i2\pi\left(x\,k_x + y\,k_y + (\Delta f_m + \psi(x,y))\cdot k_f\right)} dx\,dy \\ &= \sum_{m=1}^{M} \int \left(\int \rho_m(x,y) e^{-i2\pi\left(x\,k_x + (\Delta f_m + \psi(x,y))\cdot k_f\right)} dx \right) e^{-i2\pi y\,k_y}\,dy \quad \text{(A.1)} \end{aligned}$$

where k_f for an echo n can be described as $k_f = \mathrm{TE}_n + \tau_n = \mathrm{TE}_n + \alpha_n k_x$, with τ_n the time between each sampling time and the echo time of the acquisition. Assuming the same time map for each k-space line (such as in cartesian acquisitions) and applying an inverse Fourier transform in the "y" direction to A.1,

$$\begin{aligned} g(k_x, y') &= \mathcal{F}_y^{-1}\left\{S(k_x,k_y)\right\} = \int S(k_x,k_y) e^{i2\pi k_y y'}\,dk_y \\ &= \sum_{m=1}^{M} \iiint \rho_m(x,y) e^{-i2\pi(x\,k_x + (\Delta f_m + \psi(x,y))\cdot(T_E + \alpha k_x))} e^{-i2\pi y\,k_y} e^{i2\pi k_y y'}\,dx\,dy\,dk_y \\ &= \sum_{m=1}^{M} \iint \rho_m(x,y) e^{-i2\pi(x\,k_x + (\Delta f_m + \psi(x,y))\cdot(T_E + \alpha k_x))} \left(\int e^{-i2\pi(y-y')\,k_y}\,dk_y \right) dx\,dy \\ &= \sum_{m=1}^{M} \iint \rho_m(x,y) e^{-i2\pi(x\,k_x + (\Delta f_m + \psi(x,y))\cdot(T_E + \alpha k_x))}\,\delta(y-y')\,dx\,dy \\ &= \sum_{m=1}^{M} \int \rho_m(x,y') e^{-i2\pi(x\,k_x + (\Delta f_m + \psi(x,y'))\cdot(T_E + \alpha k_x))} dx \end{aligned}$$

which leads to a much simpler 1D optimization in a row by row basis. The objective function described in Eq. 2.1 can be used for every row.

APPENDIX B. GRADIENTS OF THE OBJECTIVE FUNCTION

For each optimization variable, the gradient function was explicitly calculated. If S^a and S^e correspond to the acquired and estimated signals, respectively, the gradient of the objective function f towards a certain variable v is the following:

$$\begin{aligned}
\frac{\partial f}{\partial v} &= \frac{\partial}{\partial v} \left\| S^a - S^e \right\|^2 \\
&= 2 \cdot \frac{\partial}{\partial v} (S^a - S^e) \cdot (S^a - S^e)^* \\
&= -2 \cdot \left((S^a - S^e) \cdot \frac{\partial S^{e*}}{\partial v} + (S^a - S^e)^* \cdot \frac{\partial S^e}{\partial v} \right) .
\end{aligned}$$

The partial derivates for each variable are

$$\begin{aligned}
\frac{\partial S^e}{\partial \rho_{m,\mathbf{r}}} &= e^{-i2\pi\left((\Delta f_m + \tilde{\psi}_{\mathbf{r}}) \cdot q + \mathbf{r}\, k_q\right)} \\
\frac{\partial S^e}{\partial \psi_{\mathbf{r}}} &= -i2\pi\, q \sum_{m=1}^{M} \rho_{m,\mathbf{r}}\; e^{-i2\pi\left((\Delta f_m + \tilde{\psi}_{\mathbf{r}}) \cdot q + \mathbf{r}\, k_q\right)} \\
\frac{\partial S^e}{\partial R_{2,\mathbf{r}}} &= -q \cdot \sum_{m=1}^{M} \rho_{m,\mathbf{r}}\; e^{-i2\pi\left((\Delta f_m + \tilde{\psi}_{\mathbf{r}}) \cdot q + \mathbf{r}\, k_q\right)} .
\end{aligned}$$

All these results are within a single acquisition.

APPENDIX C. GLOSSARY OF TERMS AND ABBREVIATIONS

Artifacts	Error in the representation of the image due to reasons apart from noise.
Chemical Shift	Deviation of a given chemical species from the nominal frequency due to magnetic shielding of the orbiting electrons. This value depends on the main magnetic field strength. In gradient echo images, it produces a displacement in the spatial domain. It is usually denoted as Δf_m for a species m.
Field inhomogeneity	The local deviation from the nominal resonance frequency, typically given by the resonance frequency of water or tetramethylsilane $Si(CH_3)_4$. It is usually denoted with the letter ψ.
FIRST	Field Inhomogeneity, R_2^* and Species estimation using a variable Time map.
Flip Angle	Change in the direction of the net magnetization vector with respect to the direction of the net magnetic field produced by a radiofrequency pulse.
FOV	Field of View.
FT	Fourier transform. A fast algorithm for calculating a discrete fourier transform is called FFT.
Gradient	May refer to two concepts: the rate of change of a certain quantity or function, or the magnetic field gradient, applied to encode the k-spacedata in a certain way.
GRE	Gradient Echo.
IDEAL	Iterative Decomposition of water and fat with Echo Assymetry and Least squares estimation.
k-space	Mathematical space in which the MR signal is sampled and represented. In perfect conditions, it represents the Fourier transform of the image.
MR	Magnetic Resonance.

MRI	Magnetic Resonance Imaging.
RF	Radiofrequency.
Resonance frequency	Also known as the Larmor frequency, it is the frequency measured in Hertz at which the spins precess given a certain magnetic field strength. The frequency and field strength are related by the equation $f = \gamma/2\pi B$, with γ the gyromagnetic ratio and B the field strength. For hydrogen atoms, the Larmor frequency has a value of 42.57 MHz.
R_2^*	Single effective transverse relaxation rate, defined as the reciprocal of the effective transverse relaxation time, T_2^*.
SNR	Signal to Noise Ratio.
TE	Echo time. Time between the excitation phase and the middle of the acquisition time.
Time map	Times where the data is sampled. Also referred as acquisition time or k_f.
TR	Repetition time. Time required to perform an entire pulse sequence, usually given by the time between two excitation pulses.
Trajectory	The path taken in the k-space domain to acquire data. It is determined by the applied gradients during the acquisition.
1D	One-dimensional.
2D	Two-dimensional.